trials with favorable safety and immunogenicity outcomes (*40*). Future studies will need to address the minimal doses of mini-HA and adjuvant for a protective response. Because preexisting immunity may have a profound effect on the breadth of the response and no animal model recapitulates the complex preexisting immunity against influenza found in humans, such studies should be performed in humans (*41*).

Concluding remarks

We have described the design and characterization of a series of soluble HA immunogens solely composed of the HA stem. Although all selected mini-HAs elicited comparable levels of antibodies to FL HA, the breadth and protective ability of the elicited antibodies progressively increased with the structural evolution of mini-HA configuration. The final candidate—stabilized trimeric mini-HA #4900—demonstrated its unique ability to elicit broad and protective immune response in mice and nonhuman primates. It has been reported (*42*, *43*) that stabilization of respiratory syncytial virus F antigen improves immune response and protection. Our results demonstrate that the same principle holds for influenza HA and provide further direction for the design of an epitope-based, universal influenza vaccine.

REFERENCES AND NOTES

1. D. Corti *et al.*, *Science* **333**, 850–856 (2011).
2. M. Throsby *et al.*, *PLOS ONE* **3**, e3942 (2008).
3. C. Dreyfus *et al.*, *Science* **337**, 1343–1348 (2012).
4. D. C. Ekiert *et al.*, *Science* **324**, 246–251 (2009).
5. D. C. Ekiert *et al.*, *Science* **333**, 843–850 (2011).
6. R. H. Friesen *et al.*, *Proc. Natl. Acad. Sci. U.S.A.* **111**, 445–450 (2014).
7. J. Sui *et al.*, *Nat. Struct. Mol. Biol.* **16**, 265–273 (2009).
8. A. Kashyap *et al.*, *Proc. Natl. Acad. Sci. U.S.A.* **105**, 5986–5991 (2008).
9. D. R. Burton, P. Poignard, R. L. Stanfield, I. A. Wilson, *Science* **337**, 183–186 (2012).
10. G. L. Chen, K. Subbarao, *Nat. Med.* **15**, 1251–1252 (2009).
11. D. C. Ekiert, I. A. Wilson, *Curr. Opin. Virol.* **2**, 134–141 (2012).
12. T. T. Wang, P. Palese, *Nat. Struct. Mol. Biol.* **16**, 233–234 (2009).
13. T. T. Wang, P. Palese, *Science* **333**, 834–835 (2011).
14. M. Kanekiyo *et al.*, *Nature* **499**, 102–106 (2013).
15. R. Hai *et al.*, *J. Virol.* **86**, 5774–5781 (2012).
16. N. Pica *et al.*, *Proc. Natl. Acad. Sci. U.S.A.* **109**, 2573–2578 (2012).
17. A. Schneemann *et al.*, *J. Virol.* **86**, 11686–11697 (2012).
18. D. Eggink, P. H. Goff, P. Palese, *J. Virol.* **88**, 699–704 (2014).
19. J. Cohen, *Science* **341**, 1171 (2013).
20. J. J. Skehel, M. D. Waterfield, *Proc. Natl. Acad. Sci. U.S.A.* **72**, 93–97 (1975).
21. I. A. Wilson, J. J. Skehel, D. C. Wiley, *Nature* **289**, 366–373 (1981).
22. J. J. Skehel *et al.*, *Proc. Natl. Acad. Sci. U.S.A.* **79**, 968–972 (1982).
23. G. Bommakanti *et al.*, *Proc. Natl. Acad. Sci. U.S.A.* **107**, 13701–13706 (2010).
24. G. Bommakanti *et al.*, *J. Virol.* **86**, 13434–13444 (2012).
25. Y. Lu, J. P. Welsh, J. R. Swartz, *Proc. Natl. Acad. Sci. U.S.A.* **111**, 125–130 (2014).
26. V. V. Mallajosyula *et al.*, *Proc. Natl. Acad. Sci. U.S.A.* **111**, E2514–E2523 (2014).
27. See supplementary materials on *Science* Online.
28. CR9114 and CR6261 share a nearly identical epitope formed by helix A of HA2 and a segment of HA1, and both neutralize virtually all group 1 influenza A strains. CR9114 also neutralizes influenza A group 2 viruses and binds influenza B strains, demonstrating greater breadth relative to CR6261. Because CR6261 appears to have more stringent epitope requirements than CR9114, we used CR6261 binding as the key criterion for the selection of final candidates.
29. The apparent importance of the glycans may partially explain why previously reported HA stem–derived proteins that were expressed in *E. coli*, and thus not glycosylated, failed to mimic the native HA stem more closely.
30. SEC-MALS analysis of mini-HAs in combination with Fab of bnAb CR8020, specific for influenza group 2 viruses, showed neither peak shift nor change in retention time for any of the proteins.
31. L. Konermann, J. Pan, Y. H. Liu, *Chem. Soc. Rev.* **40**, 1224–1234 (2011).
32. H. Wei *et al.*, *Drug Discov. Today* **19**, 95–102 (2014).
33. Structural differences between the stems of group 1 and group 2 HAs restrict the activity of most bnAbs to one group. Although some antibodies, like CR9114, can bind both groups, such antibodies appear to be extremely rare. The observed lower reactivity to group 2 HAs of immune serum elicited against group 1 HA stem mimics was therefore to be expected.
34. I. Alberini *et al.*, *Vaccine* **27**, 5998–6003 (2009).
35. D. J. DiLillo, G. S. Tan, P. Palese, J. V. Ravetch, *Nat. Med.* **20**, 143–151 (2014).
36. Z. J. Cheng *et al.*, *J. Immunol. Methods* **414**, 69–81 (2014).
37. B. S. Parekh *et al.*, *MAbs* **4**, 310–318 (2012).
38. A. Schnueriger *et al.*, *Mol. Immunol.* **48**, 1512–1517 (2011).
39. The reduction in fever in #4900-vaccinated animals relative to PBS-immunized animals is significant when periods shortly after challenge (e.g., 0 to 3 days or 0 to 8 days) are considered, because the fever is most pronounced shortly after challenge. Although still visible when the entire 21-day follow-up period is considered, the reduction is no longer statistically significant because of the large variation in measured body temperatures.
40. R. J. Cox *et al.*, *Vaccine* **29**, 8049–8059 (2011).
41. R. Roozendaal *et al.*, *PLOS ONE* **9**, e103550 (2014).
42. B. E. Correia *et al.*, *Nature* **507**, 201–206 (2014).
43. J. S. McLellan *et al.*, *Science* **342**, 592–598 (2013).

ACKNOWLEDGMENTS

We thank R. Vogels, R. van der Vlugt, D. Zuijdgeest, N. Kroos, V. Klaren, S. Schmit-Tillemans, L. Kil, S. Barens, and O. Diefenbach for scientific input and technical support; J. Klap, M. Koldijk, and G. J. Weverling for statistical support; Algonomics for input in early designs; Novavax for supplying Matrix-M; Promega for early access to mouse surrogate ADCC assay; E. Montomoli, D. Perini, and S. Piccirella from VisMederi for pseudoparticle assay; Janssen Diagnostics for quantitative polymerase chain reaction of tracheal swabs; P. Mooij and G. Koopman of the Biomedical Primate Research Center (BPRC), TNO Triskelion, Central Veterinary Institute, and PreClinBiosystems AG for performing the animal studies; and L. Dolfing and A. Dingemans for critical reading of the manuscript. The data presented in this manuscript are tabulated in the main paper and in the supplementary materials. X-ray diffraction data sets were collected at the Stanford Synchrotron Radiation Lightsource (SSRL) beamline 12-2. Use of the SSRL, SLAC National Accelerator Laboratory, is supported by the U.S. Department of Energy (DOE), Office of Science, Office of Basic Energy Sciences under contract no. DE-AC02-76SF00515. The SSRL Structural Molecular Biology Program is supported by the DOE Office of Biological and Environmental Research and by National Institute of General Medical Sciences (NIGMS) grants including P41GM103393. The contents of this publication are solely the responsibility of the authors and do not necessarily represent the official views of NIGMS or NIH. Coordinates and structure factors of the crystal structures are deposited in the Protein Data Bank as entries 5CJQ and 5CJS. Crucell Holland B.V., a Janssen company, has the following pending patent applications in this field: WO 2013/079473, WO 2014/191435, WO2008/028946, WO2013/007770, U.S. 62/062,746, and U.S. 62/062,754. Sharing of materials will be subject to standard material transfer agreements.

SUPPLEMENTARY MATERIALS

www.sciencemag.org/content/349/6254/1301/suppl/DC1
Materials and Methods
Figs. S1 to S8
Tables S1 to S3
References (*44*–*65*)

26 November 2014; accepted 29 July 2015
Published online 24 August 2015
10.1126/science.aac7263

REPORTS

METALLIC GLASSES

HPSTAR 0117—2015

Fractal atomic-level percolation in metallic glasses

David Z. Chen,[1]* Crystal Y. Shi,[2]† Qi An,[3]† Qiaoshi Zeng,[4,5] Wendy L. Mao,[2,6] William A. Goddard III,[3] Julia R. Greer[1,7]

Metallic glasses are metallic alloys that exhibit exotic material properties. They may have fractal structures at the atomic level, but a physical mechanism for their organization without ordering has not been identified. We demonstrated a crossover between fractal short-range (<2 atomic diameters) and homogeneous long-range structures using in situ x-ray diffraction, tomography, and molecular dynamics simulations. A specific class of fractal, the percolation cluster, explains the structural details for several metallic-glass compositions. We postulate that atoms percolate in the liquid phase and that the percolating cluster becomes rigid at the glass transition temperature.

Freeze a liquid fast enough, and it becomes a glass, a material that is structurally similar to the liquid but incapable of flow. This concept, albeit not well understood (*1*, *2*), is so ubiquitous that it holds even for metals (*3*). Vitrified metals, or metallic glasses, are a class of disordered materials with nondirectional bonding and possess a suite of lucrative mechanical properties, such as high elastic limit and strength (*4*). Unlike most crystalline metals and alloys, metallic glasses earn their name from a lack of long-range atomic order and the absence of typical defects, such as dislocations, rendering their microstructure challenging to conceptualize

and model. Some studies suggest the existence of short-range order, for which solute-centered clusters serve as the building blocks, and medium-range order characterized by cluster packing (*5*–*7*). These short- and medium-range packing schemes inevitably break down over longer coordinates as a result of spatial incompatibility, and they do not fully describe the atomic organization within these complex glasses. The incomplete understanding of atomic-level structure in glassy materials has made it challenging to capture the physics of their response to mechanical deformation. We propose a model that describes a short-range order and encompasses the long-range structural details of metallic glasses. The model has considerable implications for understanding glass properties and the origin of the glass transition.

Diffraction experiments characterize the structure of amorphous materials by mapping the atomic neighbor–separation distances and statistical density distributions. Dissimilar glasses and liquids commonly possess distinct short- and medium-range orders due to variations in chemical bonding, but the atomic structure becomes fluid like and nearly indistinguishable among different glasses beyond the first few nearest neighbors (*8*). The similarity of atomic-level environments in liquids and glasses makes it difficult to understand how glasses get their rigidity. Glass rigidity may be related to the jamming of atoms as density increases (*9*). The marked difference between the short- and long-range configurations in glassy systems sets glasses apart from crystals. In contrast to crystals, simplifying the underlying structure in a glass is problematic, because the short- and medium-range

[1]Division of Engineering and Applied Sciences, California Institute of Technology, Pasadena, CA 91125, USA. [2]Department of Geological Sciences, Stanford University, Stanford, CA 94305, USA. [3]Materials and Process Simulation Center, California Institute of Technology, Pasadena, CA 91125, USA. [4]Center for High Pressure Science and Technology Advanced Research, Shanghai 201203, China. [5]High Pressure Synergetic Consortium, Geophysical Laboratory, Carnegie Institute of Washington, Argonne, IL 60439, USA. [6]Stanford Institute for Materials and Energy Sciences, SLAC National Accelerator Laboratory, Menlo Park, CA 94025, USA. [7]Kavli Nanoscience Institute, California Institute of Technology, Pasadena, CA 91125, USA.
***Corresponding author. E-mail: dzchen@caltech.edu**
†These authors contributed equally to this work.

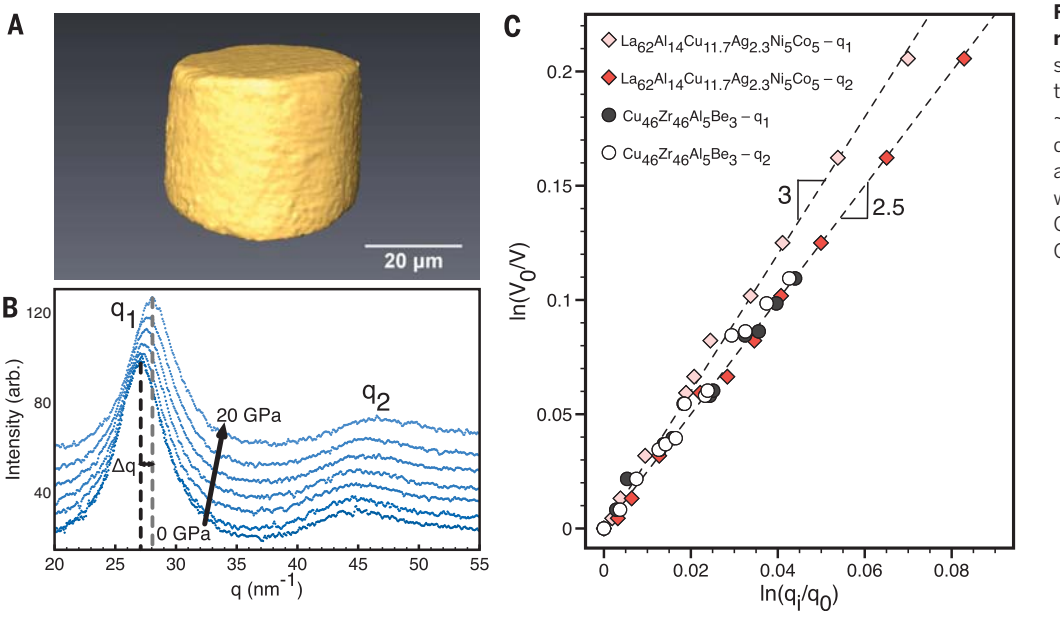

Fig. 1. In situ diffraction and volume results. (**A**) Three-dimensional reconstructed sample volumes from in situ transmission x-ray microscopy data at ~0 GPa. (**B**) In situ x-ray diffraction data with increasing pressure (arb., arbitrary units). (**C**) Volume scaling with scattering vectors $\mathbf{q_1}$ and $\mathbf{q_2}$ for $Cu_{46}Zr_{46}Al_5Be_3$ and $La_{62}Al_{14}Cu_{11.7}Ag_{2.3}Ni_5Co_5$ metallic glasses.

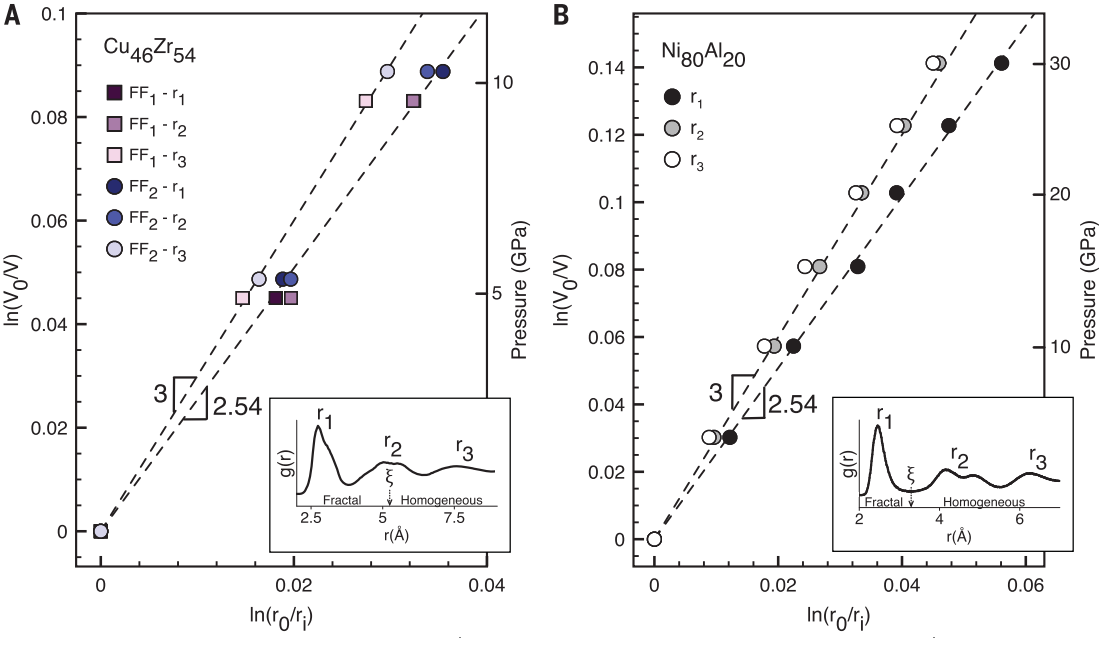

Fig. 2. Dimensionality crossover in simulations. (**A**) The $Cu_{46}Zr_{54}$ from FF_1 and FF_2 both exhibit a transition in dimensionality from ~2.5 to 3 between r_2 and r_3. (**B**) $Ni_{80}Al_{20}$ exhibits a transition in dimensionality from ~2.5 to 3 between r_1 and r_2. The insets show corresponding RDF curves with the correlation lengths ξ indicated.

orders do not repeat in a recognizable pattern. For this reason, no two glasses, produced under the same conditions and with similar diffraction patterns, are identical at the atomic level. The question of how repeatable long-range structures in glasses can emerge from nonrepeating atomic clusters remains unanswered.

Studies suggest fractal properties in metallic glasses (*10*, *11*). Fractal behavior manifests in the relationship between mass (M) and volume. For crystals, this relationship, $M(r) \sim r^3$ (where r is the radius of a region within the material), has a dimensionality (D) of 3. The dimensionality of metallic glasses is closer to ~2.5 (*11*), and any non-integer D corresponds to a fractal (*12*). Many naturally occurring random fractals have $D \sim 2.5$, including crumpled balls of paper and thin sheets (*13*), which are fractals down to the size of nanoballs of graphene oxide (*14*). Fractal concepts may be useful in developing an atomic-level understanding of amorphous materials, because they imply underlying order in inherently chaotic and random arrangements. The specific nature of fractals in metallic glasses is not obvious, because most mass fractals have macroscopic pores at large r (e.g., crumpled paper), and metallic glasses are monolithic materials. Metallic glasses have packing fractions close to or exceeding those of close-packed crystalline metals (*15*). The puzzle of how metallic glasses can simultaneously possess fractal properties and remain fully dense is unresolved (*16*). One possible explanation is that the diffraction experiments only probe the short-range dimensionality. In this work, we observed a fractal short-range $D < 3$ and a homogeneous long-range $D = 3$ for several metallic glasses, indicating the presence of a dimensionality crossover at an intermediate length scale.

Previous studies have focused on the principal (first) diffraction peak only (*10*, *11*). We extended the analysis beyond the first peak, because the information contained in diffraction experiments is spread out in momentum space, and each peak contains information that represents a part of the total structure. We conducted in situ high-pressure x-ray diffraction and full-field nanoscale transmission x-ray microscopy experiments on ~40-μm-diameter cylindrical samples of $Cu_{46}Zr_{46}Al_5Be_3$ metallic glass (Fig. 1A). We made diffraction and sample volume measurements in situ as a function of hydrostatic pressure in a diamond anvil cell. We related the scattering vector (**q**) from diffraction peak positions to volume by increasing the hydrostatic pressure from ~0 to 20 GPa (Fig. 1B). Compared with

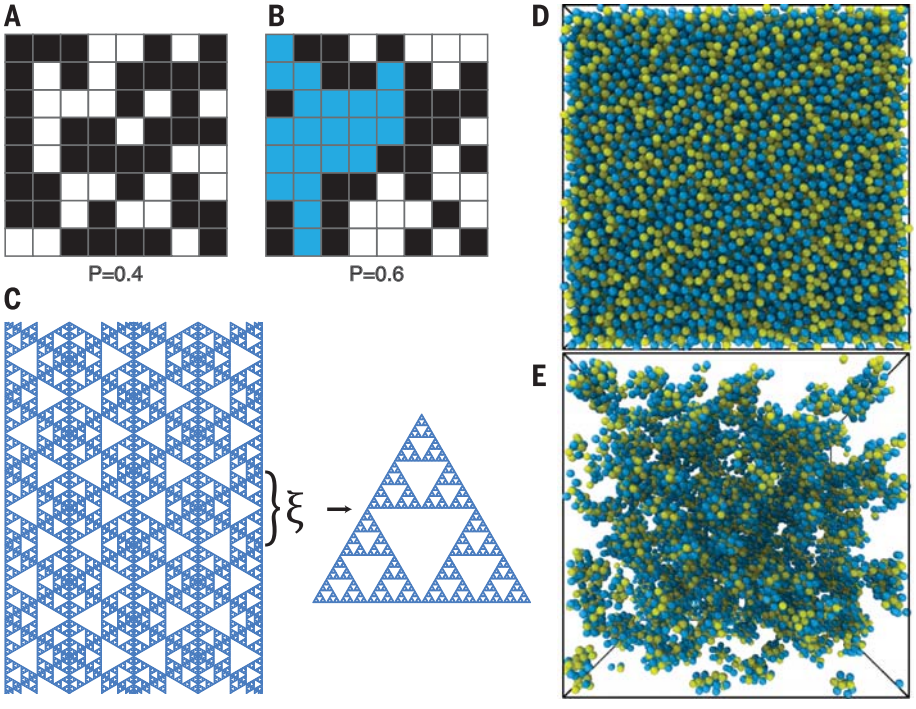

Fig. 3. Concepts in fractals and percolation. (**A** and **B**) Site lattice percolation for $p < p_c$ (A) and $p > p_c$ (B). White squares are "occupied," black squares are "unoccupied," and blue squares are percolating. (**C**) Illustrative example of a lattice made up of Sierpinski gaskets with correlation length ξ, adopted from (*23*). This lattice is fractal over the short range and homogeneous over the long range. (**D**) MD simulation of the $Cu_{46}Zr_{54}$ system at room temperature with full periodic boundaries (Cu, blue; Zr, yellow). (**E**) $Cu_{46}Zr_{54}$ with all atoms removed, except for those belonging to icosahedrons.

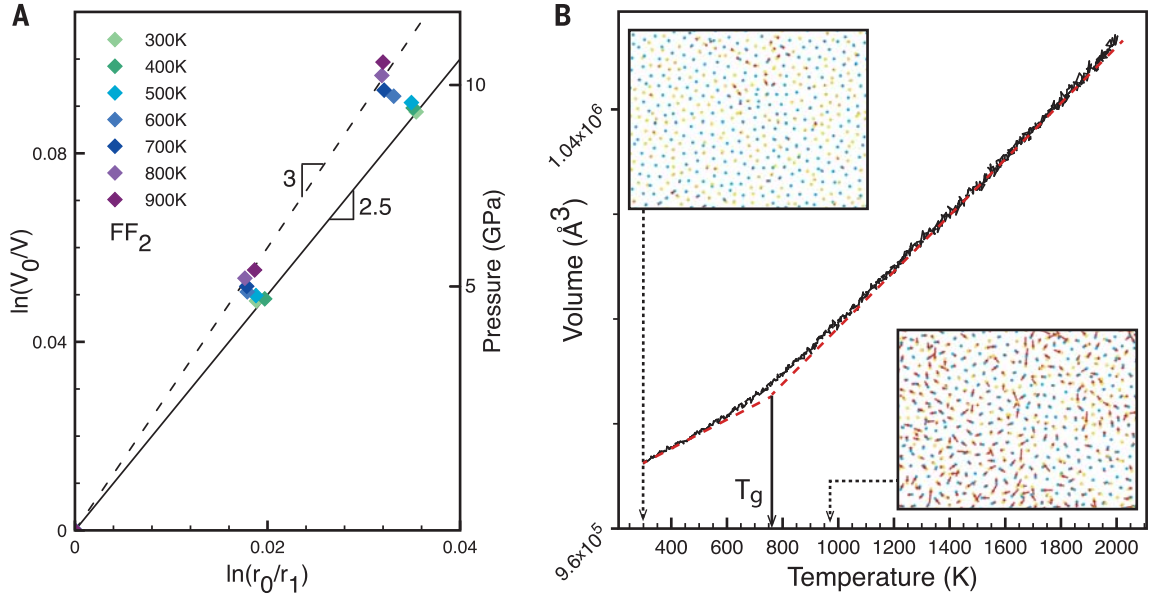

Fig. 4. Simulated properties during supercooling. (**A**) Dimensionality from r_1 during supercooling. (**B**) Volume versus temperature behavior (solid black line), shown with guidelines (red dotted line) and T_g (~763 K, solid black arrow). Inset snapshots show atom vectors (red) generated from reference temperatures ~540 K above the indicated temperatures (dotted black arrows) for a slice 3 Å thick (roughly the nearest-neighbor distance). Dots are atom centers (Cu, blue; Zr, yellow).

previous methods, using multiple data points improved accuracy in measuring the exponent (*10*). Structural information was sensitive to the magnitude of the scattering vector. We found that $D \sim 2.51$ for $\mathbf{q_1}$ (the scattering vector from the first peak position), consistent with previous experiments on other metallic glasses (*10*, *11*). The value of ~2.64 from $\mathbf{q_2}$ measurements was 5% higher than that from $\mathbf{q_1}$ (Fig. 1C). To explore the repeatability of this finding, we analyzed data obtained from a $La_{62}Al_{14}Cu_{11.7}Ag_{2.3}Ni_5Co_5$ metallic glass (*11*). First-peak data for both systems had the same exponent of ~2.5, whereas the $\mathbf{q_2}$ data for the $La_{62}Al_{14}Cu_{11.7}Ag_{2.3}Ni_5Co_5$ had an exponent of nearly 3 (Fig. 1C). This shift is greater than the one observed in the $Cu_{46}Zr_{46}Al_5Be_3$ system, and it supports the observation that a change in the dimensionality arises from probing different extents within the atomic structure in momentum space. Extracting structural information from momentum space measurements is difficult, because the information is spread out. Real-space radial distribution functions (RDFs) are needed, where peak positions correspond directly to atomic separations. Background noise and the limited range of $\mathbf{q}$ restrict the accuracy of Fourier transforms applied to experimental RDFs. Atomistic simulations allow for this type of investigation.

Molecular dynamics (MD) simulations can replicate the glass structure, but the simulation time scales (picoseconds) are many orders of magnitude shorter than in the experiments. We ensured that the system had sufficient time to relax at each pressure increment to address this issue. We held the loading rate constant at 50 GPa/ns (5×10^{19} Pa/s), and we allowed the system to relax for ~0.1 ns to reach thermodynamic equilibrium at each pressure interval. Higher quench rates in simulations may produce less relaxed glasses, although their structures often closely match those produced in experiments (*17*–*19*). The differences in compression rates result in quantitative discrepancies, but the qualitative and phenomenological aspects of the simulations should represent a realistic physical system. We generated $Cu_{46}Zr_{54}$ RDFs by using two embedded-atom-method force fields, described by Cheng *et al.* (FF_1) (*18*) and Mendelev *et al.* (FF_2) (*19*). The neighbor separation–volume relationship for RDF peaks r_1 and r_2 indicated a D of ~2.54, similar to the experimental result, but it transitioned to ~3 between r_2 and r_3 (Fig. 2A). We also simulated $Ni_{80}Al_{20}$, which exhibited a similar crossover between r_1 and r_2 (Fig. 2B) (*20*).

The percolation cluster (*21*) is probably the most relevant fractal model to describe the structure of metallic glasses. The cluster represents a disordered system with fractal dimension $D \sim 2.52$ and appears across many physical systems (*22*, *23*). Percolation models incorporate the probability of occupied (p) and empty ($1 - p$) sites. At low p values, the system is not fully connected (for example, as with an electrical insulator) (Fig. 3A). The percolation threshold (p_c) is reached when a percolating network forms, allowing incipient conduction. Systems characterized by large p have many conduction paths (Fig. 3B). What sets the percolation model apart is the existence of a correlation length, ξ, which characterizes the size of the finite clusters at concentrations below and above p_c. The correlation length is defined as the average distance that spans two sites within the same cluster and has units equal to the size of the smallest constituent unit in the model. At $p < p_c$ and $p > p_c$, ξ is finite, and the system is only fractal at length scales shorter than the correlation length. On length scales longer than ξ, the structure is homogeneous. This property of percolation clusters may help reconcile the notion that fractals need not exhibit self-similarity across all length scales (Fig. 3C) (*23*).

We used a continuum percolation model, where p is analogous to the atomic packing fraction (φ), and the percolation threshold is analogous to a critical volume fraction (φ_c), such that $\varphi_c = \varphi p_c$ (*23*, *24*). The correlation length is

$$\xi \propto |\varphi - \varphi_c|^{-v}$$

for continuum percolation, where $v = 0.8764$ (*25*).

We estimated φ_{CuZr} to be 0.717 to 0.728 using the chemical compositions and the atomic radii of the simulated glasses (*29*). A reasonable model for the packing of a binary metallic glass involves continuum packing of hard spheres, with a p_c of ~0.310 (*26*). We obtained a φ_c of 0.257 by averaging the hard-sphere value ($\varphi_c \sim 0.224 = p_c\varphi_{CuZr}$) with an overlapping sphere value ($\varphi c \sim 0.2896$) (*27*), because atoms in metallic glass are not ideally rigid (*28*). The correlation length was ~2 for $Cu_{46}Zr_{54}$ ($\xi_{CuZr} \sim 1.93$ to 1.98), suggesting that the information in the first and second peaks pertains mostly to the angstrom-sized fractal clusters, whereas information in the third peak pertains to the homogeneous bulk. This result is consistent with our observations of a crossover in dimensionality between r_2 and r_3 (Fig. 2A), and it provides evidence for the presence of percolation structure in metallic glasses. The short-range considerations for high local densities favor the formation of Cu-centered clusters, giving rise to a large number of Cu-centered icosahedra in lieu of the close-packed structures in native Cu and Zr (Fig. 3D) (*16*). The atoms with local icosahedral order form a percolating network (Fig. 3E).

Equation 1 suggests that higher packing fractions bring about shorter correlation lengths. We estimated that the $Ni_{80}Al_{20}$ has a high packing fraction, φ_{NiAl}, of ~0.793, although this could be an overestimation due to the covalent nature of the Al bonding. This estimate gives $\xi_{NiAl} \sim 1.73$, which is much less than 2. The result shows a crossover in dimensionality from ~2.54 to ~3 that occurs between r_1 and r_2 (Fig. 2B). We were also able to induce a shift in the $Cu_{46}Zr_{54}$ crossover from between r_2 and r_3 to between r_1 and r_2 at a pressure of >15 GPa by increasing the packing fraction and bringing ξ_{CuZr} below ~1.7 (fig. S1) (*29*). Some of the atoms in amorphous materials undergo local nonaffine displacements, even in response to purely hydrostatic loads. The fraction of such nonaffine atoms is low (~21.7%), and they do not appear to have any effect on the scaling behavior and crossover (figs. S2 and S3) (*29*).

We related the current model to the glass transition by examining the dimensionality as a function of temperature. We did not observe fractal behavior of $Cu_{46}Zr_{54}$ until 400 K, well below the glass transition temperature (T_g) of 763 K (Fig. 4A). The dimensionality gradually decreased from ~3 to ~2.54 over this temperature range as the temperature decreased. This behavior suggests an intermediary process such as jamming (*9*, *30*, *31*), where the percolating cluster begins to jam at the glass transition. Complete jamming occurs at lower temperatures, along with the emergence of fractal properties, correlating with a loss of ergodicity and consistent with the characteristic kink in the volume-temperature curve during supercooling (Fig. 4B). Despite structural similarities, liquids are amenable to rearrangements in local atomic configurations, whereas in rigid solids, these configurations are preserved. Pressure elicits a mostly nonaffine response from the liquid and a comparatively affine response from the glass. Applied hydrostatic forces inevitably alter the structure and induce structural relaxation in a liquid, which is unavailable in a glass. This difference is probably the reason for the emergence of fractal properties below T_g in a glass and the lack thereof above T_g in a liquid. Metallic liquids possess packing fractions in excess of our estimated percolation threshold, which implies that their atomic structures are also percolating clusters that have not yet frozen or jammed.

A fractal model might be useful in explaining the dynamics of metallic glasses, as concepts from percolation have been applied successfully to other glass formers (*32*). The dynamic heterogeneities that emerge in supercool liquids may be related to the spatial distribution of nonpercolating clusters. Estimating the average number of particles in these clusters using $\sim N_{avg} \approx \xi^3$, where $\xi \sim 2$, we got a value (~8) that is close to experimentally observed values in colloidal glasses (~3 to 7) (*33*). From the perspective of packing, percolation, and jamming, a correlation between density and T_g (*34*) is intuitive. If metallic glasses are created from the jamming of a percolating cluster, then glass formation is simplified: Liquid metal only needs to reach the jamming packing fraction, φ_j, before nucleation occurs. This could be accomplished by a combination of hydrostatic pressure and fast cooling rates. The strong correlation of metallic-glass yield strength with T_g implies that collective atomic motions dictate both yielding and glass formation (*35*). Because denser metallic glasses tend to be better glass formers with higher T_g (*34*), the strength enhancement observed in glasses with higher T_g may originate from the size of the percolating clusters, which increases with packing fraction. Higher packing leads to larger jammed clusters, which present more substantial barriers to the initiation of collective atomic motions that lead to catastrophic shear banding. The movement of

finite nonpercolating clusters may also be related to shear transformation zones, which are collective rearrangements of atoms during the deformation of metallic glasses (*36*). This concept is supported by the observation that typical zone sizes (~10 to 20 atoms) (*37*–*39*) are close to cluster sizes (~8 atoms). The continuum percolation model illustrates how structure and rigidity may organize in the absence of ordering; atoms percolate in the liquid, and the percolating cluster "freezes" (or jams) into a glass.

REFERENCES AND NOTES

1. C. A. Angell, *Science* **267**, 1924–1935 (1995).
2. P. G. Debenedetti, F. H. Stillinger, *Nature* **410**, 259–267 (2001).
3. W. Klement, R. H. Willens, P. Duwez, *Nature* **187**, 869–870 (1960).
4. M. F. Ashby, A. L. Greer, *Scr. Mater.* **54**, 321–326 (2006).
5. D. B. Miracle, *Nat. Mater.* **3**, 697–702 (2004).
6. H. W. Sheng, W. K. Luo, F. M. Alamgir, J. M. Bai, E. Ma, *Nature* **439**, 419–425 (2006).
7. A. Hirata *et al.*, *Nat. Mater.* **10**, 28–33 (2011).
8. J. Sietsma, B. J. Thijsse, *J. Non-Cryst. Solids* **135**, 146–154 (1991).
9. A. S. Keys, A. R. Abate, S. C. Glotzer, D. J. Durian, *Nat. Phys.* **3**, 260–264 (2007).
10. D. Ma, A. D. Stoica, X. L. Wang, *Nat. Mater.* **8**, 30–34 (2009).
11. Q. Zeng *et al.*, *Phys. Rev. Lett.* **112**, 185502 (2014).
12. B. B. Mandelbrot, *The Fractal Geometry of Nature (Updated and Augmented Edition)* (W.H. Freeman, New York, 1983).
13. T. Tallinen, J. A. Åström, J. Timonen, *Nat. Mater.* **8**, 25–29 (2009).
14. X. Ma, M. R. Zachariah, C. D. Zangmeister, *Nano Lett.* **12**, 486–489 (2012).
15. D. B. Miracle, *Acta Mater.* **61**, 3157–3171 (2013).
16. Y. Q. Cheng, E. Ma, *Prog. Mater. Sci.* **56**, 379–473 (2011).
17. G. Duan *et al.*, *Phys. Rev. B* **71**, 224208 (2005).
18. Y. Q. Cheng, E. Ma, H. W. Sheng, *Phys. Rev. Lett.* **102**, 245501 (2009).
19. M. I. Mendelev *et al.*, *Philos. Mag.* **89**, 967–987 (2009).
20. G. P. Purja Pun, Y. Mishin, *Philos. Mag.* **89**, 3245–3267 (2009).
21. V. K. S. Shante, S. Kirkpatrick, *Adv. Phys.* **20**, 325–357 (1971).
22. M. Sahimi, *Applications of Percolation Theory* (Taylor & Francis, Bristol, PA, 1994).
23. A. Bunde, S. Havlin, *Fractals and Disordered Systems* (Springer-Verlag, New York, 1991).
24. H. Scher, R. Zallen, *J. Chem. Phys.* **53**, 3759 (1970).
25. J. Wang, Z. Zhou, W. Zhang, T. M. Garoni, Y. Deng, *Phys. Rev. E Stat. Nonlin. Soft Matter Phys.* **87**, 052107 (2013).
26. M. J. Powell, *Phys. Rev. B* **20**, 4194–4198 (1979).
27. C. D. Lorenz, R. M. Ziff, *J. Chem. Phys.* **114**, 3659 (2001).
28. A. S. Clarke, J. D. Wiley, *Phys. Rev. B Condens. Matter* **35**, 7350–7356 (1987).
29. Materials and methods are available as supplementary materials on *Science* Online.
30. A. J. Liu, S. R. Nagel, *Nature* **396**, 21–22 (1998).
31. V. Trappe, V. Prasad, L. Cipelletti, P. N. Segre, D. A. Weitz, *Nature* **411**, 772–775 (2001).
32. R. Orbach, *Science* **231**, 814–819 (1986).
33. E. R. Weeks, J. C. Crocker, A. C. Levitt, A. Schofield, D. A. Weitz, *Science* **287**, 627–631 (2000).
34. Y. Li, Q. Guo, J. A. Kalb, C. V. Thompson, *Science* **322**, 1816–1819 (2008).
35. B. Yang, C. T. Liu, T. G. Nieh, *Appl. Phys. Lett.* **88**, 221911 (2006).
36. M. L. Falk, J. S. Langer, *Phys. Rev. E Stat. Phys. Plasmas Fluids Relat. Interdiscip. Topics* **57**, 7192–7205 (1998).
37. M. L. Falk, *Phys. Rev. B* **60**, 7062–7070 (1999).
38. A. C. Lund, C. A. Schuh, *Acta Mater.* **51**, 5399–5411 (2003).
39. F. Delogu, *Phys. Rev. Lett.* **100**, 255901 (2008).

ACKNOWLEDGMENTS

Diffraction data and simulated RDFs are available as supplementary materials. The authors thank D. C. Hofmann for providing the $Cu_{46}Zr_{46}Al_5Be_3$ wires and Y. Lin for her aid in sample loading. The authors acknowledge the financial support of the U.S. Department of Energy Office of Basic Energy Sciences (DOE-BES) and NASA's Space Technology Research Grants Program (Early Career Faculty grants to J.R.G.). W.L.M. and C.Y.S. acknowledge support from NSF grant EAR-1055454. Q.Z. acknowledges support from DOE-BES (grant DE-FG02-99ER45775) and the National Natural Science Foundation of China (grant U1530402). Portions of this work were performed at the High Pressure Collaborative Access Team (HPCAT) of the Advanced Photon Source (APS), Argonne National Laboratory. HPCAT operations are supported by DOE's National Nuclear Security Administration (NNSA) under award no. DE-NA0001974 and by DOE-BES under award no. DE-FG02-99ER45775, with partial instrumentation funding by NSF grant MRI-1126249. APS is supported by DOE-BES under contract no. DE-AC02-06CH11357. Portions of this research were carried out at the Stanford Synchrotron Radiation Lightsource, a directorate of SLAC National Accelerator Laboratory and an Office of Science User Facility operated for DOE by Stanford University. Some computations were carried out on the Shared Heterogeneous Cluster computers (Caltech Center for Advanced Computing Research) provided by the NNSA Predictive Science Academic Alliance Program at Caltech (grant DE-FC52-08NA28613) and on the NSF Center for Science and Engineering of Materials computer cluster (grant DMR-0520565). Q.A. and W.A.G. received support from the Defense Advanced Research Projects Agency–Army Research Office (grant W31P4Q-13-1-0010) and NSF (grant DMR-1436985). This material is based on work supported by an NSF Graduate Research Fellowship (grant DGE-1144469). Any opinions, findings, and conclusions or recommendations expressed in the material are those of the authors and do not necessarily reflect the views of NSF.

SUPPLEMENTARY MATERIALS

www.sciencemag.org/content/349/6254/1306/suppl/DC1
Materials and Methods
Supplementary Text
Figs. S1 to S3
References (*40*–*42*)
Databases S1 to S4

14 March 2015; accepted 31 July 2015
10.1126/science.aab1233

APPLIED OPTICS

An ultrathin invisibility skin cloak for visible light

Xingjie Ni,[1]* Zi Jing Wong,[1]* Michael Mrejen,[1] Yuan Wang,[1,2] Xiang Zhang[1,2,3]†

Metamaterial-based optical cloaks have thus far used volumetric distribution of the material properties to gradually bend light and thereby obscure the cloaked region. Hence, they are bulky and hard to scale up and, more critically, typical carpet cloaks introduce unnecessary phase shifts in the reflected light, making the cloaks detectable. Here, we demonstrate experimentally an ultrathin invisibility skin cloak wrapped over an object. This skin cloak conceals a three-dimensional arbitrarily shaped object by complete restoration of the phase of the reflected light at 730-nanometer wavelength. The skin cloak comprises a metasurface with distributed phase shifts rerouting light and rendering the object invisible. In contrast to bulky cloaks with volumetric index variation, our device is only 80 nanometer (about one-ninth of the wavelength) thick and potentially scalable for hiding macroscopic objects.

A cloak is a device that can render objects invisible to incoming waves. Transformation optics and metamaterials provide powerful tools to build cloaking devices. Different schemes relying either on coordinate transformation (*1*–*3*) or scattering cancellation (*4*–*6*) have been studied. Although the concept was first proposed for electromagnetic waves, soon it was extended to acoustic waves (*7*), heat flows (*8*–*10*), elastic or seismic waves (*11*–*13*), and even the matter waves (*14*, *15*). A quasi–conformal mapping technique (*16*) was used to design a so-called carpet cloak that conceals an object by restoring the wavefront as if it were reflected from a flat surface. This technique relaxes the requirements of hard-to-achieve material properties and anisotropy as in the case of the original cloak, thereby making it easier to design and fabricate. Such invisibility carpet cloaks were demonstrated experimentally from microwave (*17*) to optical frequencies (*18*–*23*). Nevertheless, there are still substantial limitations in current optical cloak designs that apply the quasi–conformal mapping technique. Realization requires refractive index modulation over a large volume to avoid extremely high or low index, leading to a bulky cloak. In addition, sophisticated three-dimensional (3D) fabrication with very high spatial resolution is necessary. Therefore, it is challenging to scale up this design to macroscopic sizes. In addition, the varying index has to be less than that of the environment in certain regions (Fig. 1C), making it difficult to create a cloak that works in air. As a result, the cloak is usually embedded in a dielectric prism of higher index which, however, introduces an additional phase in the reflected light and makes the optical cloak itself visible by phase-sensitive detection.

Recent development of metasurfaces pointed out a way to manipulate the phase of a propagating wave directly. The metasurface is an optically thin layer consisting of subwavelength-sized elements that locally tailor the electromagnetic response at the nanoscale accompanied by dramatic light confinement (*24*–*30*). Metasurfaces have enabled a variety of unique phenomena and applications that cannot be achieved conventionally (*31*, *32*)—for example, negative-angle refraction in a broad

[1]NSF Nanoscale Science and Engineering Center (NSEC), University of California, Berkeley, CA 94720, USA. [2]Materials Sciences Division, Lawrence Berkeley National Laboratory, Berkeley, CA 94720, USA. [3]Department of Physics, King Abdulaziz University, Jeddah 21589, Saudi Arabia.
*These authors contributed equally to this work. **†Corresponding author. E-mail: xiang@berkeley.edu**

Fractal atomic-level percolation in metallic glasses

David Z. Chen *et al.*

Science **349**, 1306 (2015);
DOI: 10.1126/science.aab1233